



Title	Spin inversion mechanisms in O ₂ binding to a model heme compound : A perspective from nonadiabatic wave packet calculations
Author(s)	Kohei, Saito; Yuya, Watabe; Takaaki, Miyazaki; Takayanagi, Toshiyuki; Hasegawa, Jun-ya
Citation	Journal of Computational Chemistry, 41(29), 2527-2537 https://doi.org/10.1002/jcc.26409
Issue Date	2020-11
Doc URL	http://hdl.handle.net/2115/83178
Rights	This is the peer reviewed version of the following article: Saito, K, Watabe, Y, Miyazaki, T, Takayanagi, T, Hasegawa, J. Spin inversion mechanisms in O ₂ binding to a model heme compound: A perspective from nonadiabatic wave packet calculations. J Comput Chem. 2020; 41: 2527– 2537, which has been published in final form at https://doi.org/10.1002/jcc.26409 . This article may be used for non-commercial purposes in accordance with Wiley Terms and Conditions for Use of Self-Archived Versions.
Type	article (author version)
File Information	WPO2HemeRv1.pdf



[Instructions for use](#)

Spin-inversion mechanisms in O₂ binding to a model heme compound: A perspective from nonadiabatic wave packet calculations

Kohei Saito, Yuya Watabe, Takaaki Miyazaki, Toshiyuki Takayanagi*

Department of Chemistry, Saitama University, 255 Shimo-Okubo, Sakura-ku, Saitama City, Saitama 338-8570, Japan

Jun-ya Hasegawa

Institute for Catalysis, Hokkaido University, Kita 21, Nishi 10, Kita-ku, Sapporo, Hokkaido 001-0021, Japan

Abstract

Spin-inversion dynamics in O₂ binding to a model heme complex, which consisted of Fe(II)-porphyrin and imidazole, were studied using nonadiabatic wave packet dynamics calculations. We considered three active nuclear degrees of freedom in the dynamics, including the motions along the Fe–O distance, Fe–O–O angle, and Fe out-of-plane distance. Spin-free potential energy surfaces for the singlet, triplet, quintet, and septet states were developed using density functional theory calculations, and spin-orbit coupling elements were obtained from CASSCF-level electronic structure calculations. The spin-inversion mainly occurred between the singlet state and one of the triplet states due to large spin-orbit couplings and the contributions of other states were extremely small. The present quantum dynamics calculations suggested that the narrow crossing region model plays a dominant role in the O₂ binding dynamics. In addition, the one-dimensional Landau-Zener model underestimated the nonadiabatic transition probability.

Corresponding author, *E-mail*: tako@mail.saitama-u.ac.jp

1. Introduction

Binding of molecular oxygen to the Fe(II)-porphyrin center in heme protein is a biologically important reaction.^[1-3] One interesting aspect of this reaction is the change in spin during the oxygen binding process. O₂ has a triplet state with two unpaired electrons ($S = 1$, where S is the spin quantum number), whereas the ground state of deoxyheme is a quintet state with four unpaired spins ($S = 2$). This produces multiple states, namely, triplet, quintet, and septet ($S = 3$), when O₂ interacts with deoxyheme.^[2] In contrast, previous electron paramagnetic resonance and Mössbauer experiments have shown that the oxyheme product has a singlet ground state.^[4, 5] Thus, the O₂ binding reaction to heme is formally spin-forbidden. A total of four spin-multiplicity states can contribute to the binding process and at least triplet to singlet state transitions should occur to form the stable singlet oxyheme product from ³O₂ + ⁵deoxyhem. The spin-multiplicity change has also been called spin-inversion, spin flip, spin crossover, or intersystem crossing in chemistry.^[6-8] In addition, the chemical reaction phenomenon accompanying spin-multiplicity change is called “two-state reactivity” or “multi-state reactivity.”^[9-11] These spin transitions are induced by relativistic spin-orbit coupling (SOC) between different spin-multiplicity states, which is generally large for heavy elements. Thus, the SOC of Fe(II) is expected to play an essential role in O₂ binding to heme. Hereafter, we use the term “spin-inversion” to describe the spin transition.

To understand the detailed spin-inversion mechanisms in O₂ binding to heme, it is crucial to characterize the features of the potential energy surfaces for all the relevant spin-multiplicity states. Extensive electronic structure studies using *ab initio* molecular orbital wavefunction theory and density functional theory (DFT) have been performed so far in simplified heme models.^[12-36] A typical example is a Fe(II)-porphyrin complex with a proximal imidazole or a related ligand. These theoretical studies mainly focused on the energetics of equilibrium structures, O₂ binding energies, and potential energy surface features as a function of the Fe–O₂ approach distance. From the calculated interaction potentials between the Fe(II)-porphyrin complex and O₂, broad and narrow crossing region mechanisms have been proposed as spin-inversion mechanisms.^[3, 27] In the broad

crossing region mechanism, spin-inversion is assumed to occur mainly at longer Fe–O₂ distances, for which the corresponding potential energy surfaces with different spin multiplicities of the O₂-heme system are nearly degenerate. The narrow crossing region mechanism, on the other hand, assumes that specific crossing points, which should mainly occur at shorter Fe–O₂ distances, play an essential role in the overall spin-inversion processes. Although previous theoretical studies have provided important insights into the possible spin-inversion mechanism in O₂ binding to heme,^[12–36] no systematic calculation to find crossing point structures between the different spin-multiplicity states has been performed.

Recently, the mixed-spin Hamiltonian method,^[37, 38] where two potential energy surfaces with different spin multiplicities are mixed through a coupling parameter, has been employed to locate approximate spin-inversion structures between the two potential energy surfaces of the model O₂-heme complex.^[39] In this method, the approximate minimum energy crossing point structure, which is important for discussing the efficiency of the spin-inversion process, can be easily optimized as a transition state on the low-lying spin-coupled potential energy surface. A total of nine spin-inversion structures were successfully optimized for the singlet-triplet, singlet-quintet, triplet-quintet, and quintet-septet spin-inversion processes. The singlet-triplet spin-inversion points occur around a short Fe–O₂ distance region, whereas the other singlet-quintet, triplet-quintet, and quintet-septet spin-inversion points are located at longer Fe–O₂ distances.^[39] This suggests that both narrow and broad crossing mechanisms may play important roles depending on the initial spin-multiplicity state. The mixed-spin Hamiltonian method enables the calculation of the intrinsic reaction coordinate (IRC) for the spin-inversion pathway, as in the case of a single electronically adiabatic reaction. The IRC calculation showed that nuclear motions along the Fe–O–O angle and Fe out-of-plane distance (deviation of Fe from the porphyrin plane) are important along the spin-inversion IRC pathways.^[39]

In this work, we perform nonadiabatic quantum wave packet dynamics calculations to understand the spin-inversion mechanisms in O₂ binding to a model heme compound further from a dynamical perspective. Extensive theoretical studies have been performed; however, most of the studies obtained static information about the features of

the potential energy surfaces and their crossings.^[12–36, 39] Spin, nonadiabatic, and vibrational dynamics cannot be described independently due to strong SOCs in many molecular systems containing heavy elements.^[40–47] The magnitudes of the SOCs of Fe(II) (100–300 cm^{-1}) are roughly comparable to those of many low-frequency vibrational modes of the oxyheme complex. Here, we use a reduced-dimensionality model, in which only a few nuclear degrees of freedom of the target chemical system are considered in the quantum nonadiabatic wave packet calculations. For multiple potential energy surfaces, we consider 16 low-lying spin states correlating with the singlet, triplet, quintet, and septet states.

2. Computational method

Our simplified heme model consists of a Fe(II)-porphyrin complex ($\text{FeC}_{20}\text{N}_4\text{H}_{12}$) with a proximal imidazole ($\text{C}_3\text{N}_2\text{H}_4$), which we refer to as FePorIm below. We use the active coordinates R , θ , and d to describe the O_2 binding dynamics to this heme model. The definition of these coordinates is shown in Figure 1. The center of mass of the porphyrin moiety is defined as the coordinate origin in this study and R is the distance between the O_a atom of O_2 and the coordinate origin. θ is the Fe– O_a – O_b bending angle and d is the deviation distance of Fe atom from the porphyrin plane. The Fe atom, the center of mass of the PorIm moiety, and the O_a atom are always arranged in collinear configurations in the present calculations. The coordinates R , θ , and d are taken from our previous study on the IRC calculations for the spin-inversion pathways.^[39] In particular, we found that the nuclear motion along θ was important for the singlet-triplet spin-inversion because the optimized Fe– O_a – O_b angles for the singlet and triplet minimum structures were somewhat different (121° and 133° , respectively). Similarly, we found that the motion along d was an important role in the quintet-septet and quintet-singlet spin-inversion processes.^[39] The Hamiltonian of the three degrees of freedom model employed in this work is written (in atomic units) as

$$\mathcal{H}(R, \theta, d) = -\frac{1}{2\mu_R} \frac{\partial^2}{\partial R^2} - \frac{1}{2m_O r^2} \frac{\partial^2}{\partial \theta^2} - \frac{1}{2\mu_d} \frac{\partial^2}{\partial d^2} + \mathbf{V}(R, \theta, d), \quad (1)$$

where \mathbf{V} is the potential energy matrix described by the spin-diabatic representation. μ_R and μ_d are the reduced masses of the motions along the R and d coordinates, respectively. r is the O_a - O_b distance, which is taken to be a constant value ($r = 1.24 \text{ \AA}$) throughout this study. The potential energy matrix can be formally written as

$$\mathbf{V}(Q) = \begin{pmatrix} V_0(Q) & V_{01}(Q) & 0 & 0 \\ V_{01}^t(Q) & V_1(Q) & V_{12}(Q) & 0 \\ 0 & V_{12}^t(Q) & V_2(Q) & V_{23}(Q) \\ 0 & 0 & V_{23}^t(Q) & V_3(Q) \end{pmatrix}, \quad (2)$$

where Q collectively denotes the three active coordinates. Each diagonal term, $V_i(Q)$ ($i = S$, spin quantum number), is a $(2i + 1) \times (2i + 1)$ matrix whose diagonal elements are the spin-free potential energy surface for each spin-multiplicity state, whereas its nondiagonal elements are taken to be zero.^[8] By omitting the Q dependence, the SOC matrices, V_{ij} , can be written as

$$V_{01} = (z_1 \quad ib_1 \quad z_1^*), \quad (3)$$

$$V_{12} = \begin{pmatrix} z_2 & ib_2 & z_3^* & 0 & 0 \\ 0 & z_4 & ib_3 & z_4^* & 0 \\ 0 & 0 & z_3 & ib_2 & z_2^* \end{pmatrix}, \quad (4)$$

$$V_{23} = \begin{pmatrix} z_5 & ib_4 & z_6^* & 0 & 0 & 0 \\ 0 & z_7 & ib_5 & z_8^* & 0 & 0 \\ 0 & 0 & z_9 & ib_6 & z_9^* & 0 \\ 0 & 0 & 0 & z_8 & ib_5 & z_7^* \\ 0 & 0 & 0 & 0 & z_6 & ib_4 & z_5^* \end{pmatrix}, \quad (5)$$

where the matrix elements are arranged in the order of the magnetic quantum number (M_S) of the spin quantum number (S).^[8] z_i , z_i^* , and b_i denote a complex value, its conjugate,

and a real value, respectively. Here, we can safely ignore the SOCs with $|\Delta S| > 1$ or $|\Delta M_S| > 1$. Thus, the total potential energy matrix in Eq. (2) becomes a (16×16) Hermitian matrix.

The spin-free potential energy surfaces for the four different spin quantum numbers are obtained from the unrestricted DFT calculations using the B97D functional. We use the standard 6-311+G* basis sets for Fe and O atoms, and the 6-31G** basis sets for C, N, and H atoms, as in our previous work.^[39] The B97D calculations are done at the grid points described by the three coordinates R , θ , and d , where the structure of the PorIm part is taken from the optimized structure of the isolated FePorIm in the lowest quintet state. Twenty-seven points are used for R in the range of 1.5–6 Å. Eleven points are chosen for θ in the range of 80–150°, whereas 13 points in the range of -0.4 – 0.4 Å are used for d . A total of 3,861 points are generated and all the calculations are performed using the Gaussian09 package program.^[48] We perform the B97D calculations so that the R coordinate of the O₂-FePorIm system becomes the Z-axis of the Cartesian coordinates. The standard cubic spline interpolation technique is used to obtain desired potential energy values at a given set of three coordinates. For the θ and d coordinates, potential energy values outside the grid points are extrapolated using quadratic potentials whose polynomial parameters are determined from the grid data in the edge region. These quadratic potentials are used so that the wave packet dynamics occur mainly within the above potential energy surface region.

Figure 2(a) displays the one-dimensional potential energy curves for all four different spin quantum numbers as a function of R , which corresponds to the distance between the Fe position and the coordinate origin. The other two coordinates, namely, θ and d , are fully optimized with respect to energy at a fixed value of R . These potential energy curves correspond to the diagonal terms of the potential energy surface matrix of Eq. (2). For the triplet, quintet, and septet states, the potential energies are slightly shifted so that these three potential energy curves asymptotically become exactly degenerate. The nondegenerate behavior of the original DFT calculations comes from energetic errors of the unrestricted DFT formalism. The shifted energy values are smaller than 0.13 eV. Similarly, the potential energy surface for the singlet state is also shifted so that the

asymptotic energy difference between the singlet and other states is 5.5 kcal/mol (= 0.24 eV). This value is determined from the previous best estimate (4.6–6.5 kcal/mol), which was obtained from the high-level CASPT2 calculations.^[49] The triplet potential energy curve shows a double well feature. These two potential wells correspond to two different spin structures, as discussed in previous papers.^[29, 39] For the potential well at a longer region, O₂ has an original triplet character, even in the O₂-FePorIm complex, and thus the O₂ moiety and the FePorIm moiety have opposite spin characters (i.e., α - and β -spin, respectively). In contrast, the same spin is distributed over both the O₂ and FePorIm moieties around the potential well in a shorter region due to partial electron transfer from O₂ to FePorIm. The potential energy curve for the singlet state has a potential well of ~0.24 eV, which is smaller than in our previous calculations^[39] because the FePorIm structures are always fixed in this study.

In order to further understand the quality of the present B97D-level potential energy surfaces, we have performed the strongly-contracted NEVPT2 (N-Electron Valence State Second Order Perturbation Theory)^[50] calculations using the ORCA program.^[51] The NEVPT2 method is an efficient computational method that can be applied to large systems and was shown to give comparable or better accuracy as the popular CASPT2.^[51] The comparison of the potential energy curves between the B97D and NEVPT2 results is presented in Figure S1 of Supporting Information. In these calculations, the structure of the PorIm moiety is taken from the structure optimized at the B97D level. We found that both the B97D and NEVPT2 potential energy curves have a similar attractive feature suggesting that the B97D potential energy surfaces can be used to understand the nuclear dynamics at a qualitative level. However, the NEVPT2 calculations give too large asymptotic energy differences between the singlet and other spin states. This is in high contrast with the B97D results as mentioned previously. Therefore, we have compared the potential energy curves obtained from the B97D and NEVPT2 results, which are shifted in energy so as that the asymptotic energies become identical. The comparison is presented in Figure S2 of Supporting Information. It is seen that the both potential energy curves yield spin state crossings in a similar region indicating that the B97D-level potential energy surfaces are a reasonable choice for

dynamics calculations.

Another important point obtained from the NEVPT2 calculations is that there exist low-lying excited states for the singlet and triplet states (see Figure S1). This indicates that such excited states should be taken into account in the nonadiabatic nuclear dynamics. However, those excited states are asymptotically correlated with the excited states of the isolated heme compound and the corresponding excitation energies are much larger than thermal energy. Hence the contribution of those excited states is expected to be small although those states may not be ignored in the strong interaction region. The present dynamics model thus assumes “fast internal conversion” between the same spin multiplicity states with different electronic structures and focuses only on the slower intersystem crossing dynamics.

In Figure 3, two-dimensional contour plots of the potential energy surface for each spin quantum number are shown as a function of R and θ , where three representative values are chosen for d (-0.2 , 0 , and 0.2 Å). Bold red lines in the contour plots indicate the crossing seam between the singlet and triplet potential energy surfaces. Green and blue contours correspond to the triplet-quintet and quintet-septet crossing seams, respectively. These crossing seams generally occur at shorter R regions, and thus could play an important role in the narrow crossing region mechanism.

The SOC values are calculated at some selected points because it is expected that the magnitude of SOC does not depend substantially on the structure.^[52] In this work, the SOC values are determined within the Breit–Pauli approximation (with the SOMF approximation)^[53] using the state-interacting method at the state-averaged CASSCF/def2-TZVP level of theory. These electronic structure calculations are performed using the ORCA program.^[51] Four states (singlet, triplet, quintet, and septet) are equally averaged, where eight active electrons are distributed among seven active orbitals in the CASSCF wavefunction. The active space chosen here is minimal, including five Fe $3d$ and two O₂ π^* orbitals. The active orbitals used in the CASSCF calculations are shown in Figure S3 of Supporting Information. We have also performed the CASSCF calculations at a selected heme-O₂ structure to understand the effect of higher electronic states on the calculated SOC values, where we have included a total of two singlet states

and three triplet states. The obtained results are summarized in Table S1 of Supporting Information. It is found that the magnitude of the SOC value between the lowest triplet and quintet states is not very different from the single spin state result. This trend can also be seen for the SOC between the quintet and septet states.

In Figure 4, the SOCs obtained from the state-averaged CASSCF(8_e, 7_o)/def2-TZVP calculations are plotted as a function of R with d set to zero. In this case, R is exactly the same as the Fe-O_a distance (see Figure 1). Figure 4(a) shows the SOC elements between the singlet and triplet states. The value of b_1 ($M_s = 0$, see Eq. (3)) is much larger (~ 400 cm⁻¹) than the values of z_1 ($M_s = \pm 1$). This result is quantitatively consistent with the highly accurate multi-state CASPT2 calculations,^[29] where a larger active space with larger basis sets was employed. In contrast with the singlet-triplet coupling result, the calculated SOCs between triplet and quintet and between quintet and septet states are much smaller (Figures 4(b) and 4(c)). The coupling values are essentially zero for $R \geq 3$ Å, although the corresponding values increase at shorter distances. The results presented in Figure 4 suggest that the narrow crossing region mechanism is more important than the broad crossing region mechanism in the overall spin-inversion dynamics. The θ dependence of the SOC is also examined; however, the calculated coupling values do not strongly depend on θ . Similarly, we examine the d dependence of the SOCs. The structural dependence is shown in Figure S4 of Supporting Information. The change in d affects the Fe-O_a distance ($= R + d$). Therefore, the magnitude of the SOC can be roughly described as a function of the Fe-O_a distance only. Accordingly, the θ dependence of the SOC is ignored and the overall SOC is assumed to depend on only the Fe-O_a distance in the subsequent wave packet calculations. The calculated SOC values are interpolated with the cubic spline technique to obtain a value at a desired coordinate.

Once the spin-free potential energy surfaces and nondiagonal SOC functions are obtained, we construct the total (16 × 16) potential energy surface matrix. Figure 2(b) shows the 16 adiabatic potential energy curves obtained from the diagonalization of the (16 × 16) matrix as a function R . Similar to Figure 2(a), the other two coordinates, θ and d , are fully optimized with respect to energy at a fixed value of R . The plot in the inset in Figure 2(b) shows enlarged potential energy curves in the asymptotic region. The triplet,

quintet, and septet states, which are asymptotically degenerate without SOCs, split into the states with different energies. Due to the largest coupling ($b_1 \sim 400 \text{ cm}^{-1}$) between the singlet and triplet ($M_S = 0$) states, the contribution of the triplet ($M_S = 0$) state is the most dominant for the lowest adiabatic state in the asymptotic region. In addition, the energy splitting between the lowest adiabatic state and the next adiabatic state is obtained as about 80 cm^{-1} .

The nuclear wave packet vector $\boldsymbol{\psi}(R, \theta, d; t)$ is described by solving the time-dependent Schrödinger equations as

$$i \frac{\partial}{\partial t} \boldsymbol{\psi}(R, \theta, d; t) = \mathcal{H}(R, \theta, d) \boldsymbol{\psi}(R, \theta, d; t), \quad (6)$$

where the nuclear Hamiltonian operator is given by Eq. (1). The initial wave packet at $t = 0$ is constructed with the product of the standard Gaussian wave packet and Gaussian functions as

$$\boldsymbol{\psi}(R, \theta, d; t = 0) \sim \begin{pmatrix} c_1(0) \\ c_2(0) \\ \vdots \\ c_{16}(0) \end{pmatrix} e^{-a_R(R-R_0)^2 - ikR} e^{-a_\theta(\theta-\theta_0)^2} e^{-a_d(d-d_0)^2}, \quad (7)$$

where $c_i(t = 0)$ is the initial population amplitude for the i -th diabatic state ($i = 1$ for singlet, $i = 2-4$ for triplet, $i = 5-9$ for quintet, and $i = 10-16$ for septet). k is the initial translational wave vector for the motion along R and is given by $k = (2\mu_R E)^{1/2}$, where E is collision energy. This energy corresponds to an average collision energy in the time-dependent representation due to the Gaussian width. R_0 , θ_0 , and d_0 are central positions of the initial wave packet and a_R , a_θ , and a_d are their width parameters, respectively. We use this simple functional form for the initial wave packet because the purpose of this study is to understand the nonadiabatic spin-inversion mechanism qualitatively. The time-dependent nuclear wave packet is represented using grid-based discrete-variable representations (DVRs),^[54] where the standard particle-in-a-box basis is employed for all three coordinates. Once the initial wave packet is prepared, it is propagated in time using

the extended split-operator method, which corresponds to the extension of the standard adiabatic split-operator method to the multiple potential energy surface problems.^[55–58] To avoid the artificial reflection of the wave packet at the longer edge of the grid in the R coordinate, we use a negative imaginary potential with a quadratic form. The DVR grid parameters are 256, 128, and 64 points for R , θ , and d coordinates, respectively. The total step for time propagation is 20,000–100,000 with $\Delta t = 10.0$ atomic time units depending on the average collision energy.

3. Results and discussion

Figures 5 and 6 show representative wave packet evolutions obtained from the calculations with an average collision energy of $E = 0.136$ eV ($= 0.005$ au). The initial wave packet is placed on the triplet, quintet, and septet states with an equal diabatic population ($c_1 = 0$ and $c_i = 1/15$ for $i = 2–16$). In these plots, the wave packet densities are summed over all the M_s states. The wave packets arrive at the potential well region at $t \sim 0.5$ ps. After this, the singlet state is formed. A small singlet component is visible at an earlier time of $t = 0.242$ ps (Figures 5(a) and 6(a)); however, this component comes from the initial singlet-triplet mixing due to the large b_1 SOC value. A large part of the wave packets on the triplet, quintet, and septet states moves to a large- R region at $t = 1.208$ ps, whereas part of the wave packet on the singlet state stays around the potential well even at $t = 1.208$ ps. This indicates that quantum resonance states with a longer lifetime are produced once the wave packet is trapped in the potential well. However, because the present dynamics are essentially an inelastic scattering process, the wave packet density should finally become zero due to the absorption at the edge. The results confirm that more than 99% of the wave packet density is absorbed by the negative imaginary potential within 24 ps.

The nonadiabatic spin-inversion mechanism can also be understood from the time-dependent population on each spin-multiplicity state, which corresponds to $|c_i(t)|^2$ ($i = 1–16$). Figure 7 shows the 16 population values plotted as a function of time for the

wave packet dynamics presented in Figures 5 and 6. The $i = 1$ population curve (singlet, $S = M_S = 0$), which is initially zero, shows a maximum (~ 0.03) at $t = 0.5$ ps. The population curve ($i = 3$, triplet with $M_S = 0$) shows a dip at $t = 0.5$ ps. This mirror image indicates that spin-inversion from one of the triplet states to the singlet state occurs around this time. The detailed wave packet analyses show that this behavior corresponds to the first passage dynamics around the singlet-triplet crossing region. Thus, the spin-inversion in O_2 binding to heme is an ultrafast spin-inversion process. The populations for other states are almost constant up to $t = 1$ ps, although small nonadiabatic transitions are visible for the triplet states with $M_S = \pm 1$. The change in nonadiabatic transitions for the quintet and septet states are even smaller. These results are consistent with the magnitude of SOCs shown in Figure 4. After $t = 1$ ps, all the populations gradually decay due to the absorption of the wave packet density through the negative imaginary potential in the edge region.

Based on the results presented in Figure 7, the quintet and septet states are essentially spectator states and can be safely ignored in wave packet dynamics. Therefore, we can reduce the 16-spin state dynamics to the 4-spin state dynamics, which includes only the singlet and three triplet states. This simplification substantially reduces computational time and we perform the 4-spin state dynamics calculations using many different initial conditions. The nonadiabatic dynamics do not depend strongly on the choice of the Gaussian width parameters and the initial wave packet position parameters. Instead, the initial average collision energy affects the results. Representative results are shown in Figure 8, where we plot the diabatic population evolutions calculated at four average collision energies ($E = 0.0544, 0.136, 0.218, \text{ and } 0.272$ eV). In all cases, the initial wave packet is placed on the triplet states with an equal diabatic population ($c_1 = 0$ and $c_2 = c_3 = c_4 = 1/3$). The result presented in Figure 8(b) is similar to that in Figure 7 (except for the absolute values), indicating that including the quintet and septet states does not affect the nonadiabatic dynamics. With increase in average collision energy, the earlier the time at which the nonadiabatic transition occurs. The population decay due to the negative imaginary absorption also occurs at an earlier time as the collision energy increases. These results are quite reasonable. More importantly, the nonadiabatic transition probability slightly increases as the average collision energy increases. This

behavior can be understood from the increase in the peak value of the population for $S = M_s = 0$. However, we emphasize that the present wave packet dynamics calculation cannot yield an accurate transition probability at a specific collision energy because the flux analyses cannot be applied. Such an analysis is possible if the interaction between the adiabatic states is completely ignored such as asymptotic states. In fact, the dynamics is a totally inelastic process and the incoming wave packets, which are initially located on the triplet states, finally dissociate into FePorIm + O₂ in the triplet states again because the asymptotic singlet production is energetically forbidden at low energy (see Figure 2).

In the multidimensional inelastic scattering case, we cannot obtain accurate probabilities for the singlet state production from the wave packet calculations. Nevertheless, it may be important to compare the results of the wave packet calculations with the well-known two-state Landau-Zener model. To estimate these probabilities roughly, we first perform the 4-spin state wave packet dynamics with a different initial wave packet population so that the initial wave packet population is only in the lowest adiabatic state in the asymptotic region (Figure 2(b)). This adiabatic population can be easily transformed into the spin diabatic populations using the eigenvectors of the (4×4) Hamiltonian matrix. In this case, the contribution of the triplet states with $M_s = \pm 1$ is essentially zero and only the nonadiabatic transition between the singlet and $M_s = 0$ triplet states is visible. The wave packet calculations are performed at four average collision energy values. The time-dependent populations in the two adiabatic states are plotted in Figure 9(a) as a function of time. The sum of these two adiabatic populations becomes almost unity (before the population decay starts), indicating that the dynamics can be indeed described by the two-state model (evolution of the adiabatic wave packets are also shown in Figures S5 and S6 of Supporting Information). Interestingly, we can see the plateau region of the adiabatic populations just after the first passage of the crossing region. For example, in the case of $E = 0.136$ eV, the two adiabatic population curves are found to be almost flat in the range of $t = 0.55$ – 0.75 ps. This behavior strongly suggests that these adiabatic populations are corresponding to the single-passage transition probabilities between the two states. We can also see a slight increase in the populations on the lowest adiabatic states for $E = 0.0544$ and 0.136 eV. After this, the populations are

seen to decay due to the wave packet absorption. This phenomenon suggests that the transition from the singlet to triplet states occurs before the dissociation into FePorIm + O₂. From these considerations, we can roughly estimate the singlet-triplet transition probabilities after the first passage of the crossing region from the observed plateau regions.

We can also roughly estimate the singlet production probabilities from the diabatic populations on the $S = Ms = 0$ state, which are plotted in Figure 9(b) as a function of time. The results in Figure 9(b) are similar to the results presented in Figure 8 except for the absolute value (by a factor of ~ 3). The population peak approximately corresponds to the first wave packet passage around the crossing region. We estimate the transition probability by averaging the diabatic population values in the flat region seen in the adiabatic population curve mentioned above. In this case, we have subtracted the small average initial population due to the coupling. The results of these two (adiabatic and diabatic) analyses are presented in Figure 9(c). It is interesting to note that the two analyses yield similar probabilities except for the lowest average energy. Also shown in Figure 9(c) is the transition probability calculated using the time-independent R -matrix propagation method,^[57] where the one-dimensional singlet and triplet potential energy curves along with the SOCs are used (Figures 2 and 4). In this case, the transition probability can be calculated by terminating at $R = 1.8 \text{ \AA}$, which converts an inelastic scattering problem into a reactive scattering problem (single passage scattering case since the asymptotic analysis is applied at $R = 1.8 \text{ \AA}$). The one-dimensional result shows an expected feature of the standard Landau–Zener model.^[6–8] One important conclusion is that the one-dimensional result is smaller than the wave packet result by a factor of 2–4, although our probability estimation procedures are approximate. Nevertheless, similar findings have been reported in recent theoretical studies using *ab initio* multiple spawning calculations of the spin-inversion dynamics of the GeH₂ and SiH₂ systems.^[59–61] Our group has more recently found a similar trend in the study of the ${}^3\text{Fe}(\text{CO})_4 + \text{H}_2 \rightarrow {}^1\text{FeH}_2(\text{CO})_4$ spin-inversion reaction.^[52] These theoretical studies along with the present study indicate that coupling between the nonadiabatic spin-inversion motion and other nuclear motions plays an essential role leading to multidimensional nonlocal transitions. Thus, we qualitatively

conclude that the multidimensional and nuclear quantum effects play an important role in spin-inversion processes for polyatomic systems although more systematic dynamics studies should be performed to understand the effect of missing nuclear degrees of freedom.

4. Conclusions and future directions

Understanding detailed spin-inversion mechanisms in O₂ binding to heme is a long-standing issue in biochemistry. In this work, we performed reduced-dimensionality nonadiabatic quantum wave packet calculations using a model heme compound, which consisted of Fe(II)-porphyrin and imidazole. Although we considered only three nuclear degrees of freedom and only the lowest spin-multiplicity states, we obtained a reasonable picture of the spin-inversion mechanism. The spin-inversion between the singlet state ($S = 0$) and one of the triplet spin states ($S = 1$ and $M_s = 0$) was important due to large SOC's and the other spin states with $M_s = \pm 1$ did not contribute substantially to the nonadiabatic spin-inversion dynamics. Because the spin inversion occurred mainly in a shorter Fe-O distance region of the potential energy surfaces, we concluded that the narrow crossing region model played a more important role than the broad crossing region model within the present reduced-dimensional model. However, we emphasize that this conclusion was derived from the reduced-dimensionality model. It is possible that the SOC's between higher spin-multiplicity states such as quintet and septet states may be large in different potential energy surface regions, which we did not consider in this study. In addition to this, the inclusion of more nuclear degrees of freedom in the dynamics may change the nonadiabatic mechanism due to the efficiency change of vibrational energy redistribution. More importantly, it should be emphasized that spin-orbit couplings are not always dominant interactions in intersystem crossing phenomena. Recently, even if spin-orbit couplings are small, spin-vibronic interactions, which are corresponding to the second-order terms simultaneously containing spin-orbit and vibronic couplings,^[40, 47] can play a very important role in the nonadiabatic intersystem crossing dynamics. In fact, it is found

that the spin-vibronic effect is significant in the intersystem crossing in thermally activated delayed fluorescence processes for Cu complexes.^[62] All these points should be addressed in the future to fully understand the nonadiabatic dynamics in O₂-binding to heme.

Acknowledgements

This work was supported by a Grant-in-Aid for Scientific Research from the Ministry of Education, Culture, Sports, Science and Technology of Japan (Grant No. 17KT0093).

References

- [1] S. Shaik, H. Chen, Lessens on O₂ and NO bonding to heme from ab initio multireference/multiconfiguration and DFT calculations, *J. Bio. Inorg. Chem.* **2011**, *16*, 841.
- [2] B. F. Minaev, V. O. Minaeva, H. Ågren. Spin-Orbit Coupling in Enzymatic Reactions and the Role of Spin in Biochemistry. In: Handbook of Computational Chemistry. (Editor: J. Leszczynski), 2012, Springer, Dordrecht, 1067.
- [3] K. P. Kepp, Heme: from quantum spin crossover to oxygen manager of life, *Coord. Chem. Rev.* **2017**, *344*, 363.
- [4] J. Friedman, B. Campbell, Structural dynamics and reactivity in hemoglobin. In: Protein Structure. Proceedings in Life Sciences. (Editors: R. Austin et al.), 1987, Springer, New York, 211.
- [5] B. H. Huynh, G. C. Papaefthymiou, C. S. Yen, J. L. Groves, C. S. Wu, Electronic structure of Fe²⁺ in normal human hemoglobin and its isolated subunits, *J. Chem. Phys.* **1974**, *61*, 3750.
- [6] C. M. Marian, Spin-orbit coupling and intersystem crossing in molecules, *Comp. Mol. Sci.* **2012**, *2*, 187.
- [7] J. N. Harvey, Spin-forbidden reactions: computational insight into mechanisms and kinetics, *Comp. Mol. Sci.* **2014**, *4*, 1.
- [8] A. O. Lykhin, D. S. Kaliakin, G. E. dePolo, A. A. Kuzubov S. A. Varganov, Nonadiabatic transition state theory: Application to intersystem crossings in the active sites of metal-sulfur proteins, *Int. J. Quantum Chem.* **2016**, *116*, 750.
- [9] D. Schröder, S. Shaik, H. Schwarz, Two-state reactivity as a new concept in organometallic chemistry, *Acc. Chem. Res.* **2000**, *33*, 139.
- [10] H. Hirao, D. Kumar, L. Que, S. Shaik, Two-state reactivity in alkane hydroxylation by non-heme iron-oxo complexes. *J. Am. Chem. Soc.* **2006**, *128*, 8590.
- [11] S. Shaik, H. Hirao, D. Kumar, Reactivity of high-valent iron-oxo species in enzymes and synthetic reagents: A tale of many states. *Acc. Chem. Res.* **2007**, *40*, 532.
- [12] D. A. Scherlis, D. A. Estrin, Structure and spin-state energetics of an iron porphyrin

- model: An assessment of theoretical methods, *Int. J. Quantum Chem.* **2002**, *87*, 158.
- [13] S. Franzen, Spin-dependent mechanism for diatomic ligand binding to heme, *Proc. Nat. Acad. Sci.* **2002**, *99*, 16754.
- [14] K. P. Jensen, U. Ryde, How O₂ binds to heme: reasons for rapid binding and spin inversion, *J. Bio. Chem.* **2004**, *279*, 14561.
- [15] H. Nakashima, J. Hasegawa, H. Nakatsuji, On the reversible O₂ binding of the Fe-porphyrin complex, *J. Comp. Chem.* **2006**, *27*, 426.
- [16] J. Ribas-Ariño, J. J. Novoa, The mechanism for the reversible oxygen addition to heme. A theoretical CASPT2 study, *Chem. Comm.* **2007**, 3160.
- [17] N. Strickland, J. N. Harvey, Spin-forbidden ligand binding to the ferrous-heme group: Ab initio and DFT studies, *J. Phys. Chem. B* **2007**, *111*, 841.
- [18] D. A. Scherlis, M. Cococcioni, P. Sit, N. Marzari, Simulation of heme using DFT + U: A step toward accurate spin-state energetics, *J. Phys. Chem. B* **2007**, *111*, 7384.
- [19] M. Radoń, K. Pierloot, Binding of CO, NO, and O₂ to heme by density functional and multireference ab initio calculations, *J. Phys. Chem. A* **2008**, *112*, 11824.
- [20] H. Chen, M. Ikeda-Saito, S. Shaik, Nature of the Fe–O₂ bonding in oxy-myoglobin: effect of the protein, *J. Am. Chem. Soc.* **2008**, *130*, 14778.
- [21] P. E. M. Siegbahn, M. R. A Blomberg, S.-L. Chen, Significant van der Waals effects in transition metal complexes, *J. Chem. Theo. Comp.* **2010**, *6*, 2040.
- [22] D. E. Bikiel, F. Forti, L. Boechi, M. Nardini, F. J. Luque, M. A. Martí, D. A. Estrin, Role of heme distortion on oxygen affinity in heme proteins: The protoglobin case, *J. Phys. Chem. B* **2010**, *114*, 8536.
- [23] S. R. Badu, R. H. Pink, R. H. Scheicher, A. Dubey, N. Sahoo, K. Nagamine, T. P. Das, First principles electronic structure investigation of order of singlet and triplet states of oxyhemoglobin and analysis of possible influence of muon trapping, *Hyperfine Interact.* **2010**, *197*, 331.
- [24] T. Saito, Y. Kataoka, Y. Nakanishi, T. Matsui, Y. Kitagawa, T. Kawakami, M. Okumura, K. Yamaguchi, Theoretical studies of the effect of orientation of ligands and spin contamination error on the chemical bonding in the FeO₂ core in oxymyoglobin, *J. Mol. Struct.: THEOCHEM* **2010**, *954*, 98.

- [25] M.-S. Liao, M.-J. Huang, J. D. Watts, FeP(Im)–AB bonding energies evaluated with a large number of density functionals (P = porphine, Im = imidazole, AB = CO, NO, and O₂), *Mol. Phys.* **2011**, *109*, 2035.
- [26] M. E. Ali, B. Sanyal, P. M. Oppeneer, Electronic structure, spin-states, and spin-crossover reaction of heme-related Fe-porphyrin: A theoretical perspective, *J. Phys. Chem. B* **2012**, *116*, 5849.
- [27] K. P. Kepp, O₂ binding to heme is strongly facilitated by near-degeneracy of electronic states, *ChemPhysChem* **2013**, *14*, 3551.
- [28] V. E. J. Berryman, R. J. Boyd, E. R. Johnson, Balancing exchange mixing in density-functional approximations for iron porphyrin, *J. Chem. Theo. Comp.* **2015**, *11*, 3022.
- [29] Y. Kitagawa, Y. Chen, N. Nakatani, A. Nakayama, J. Hasegawa, A DFT and multi-configurational perturbation theory study on O₂ binding to a model heme compound via the spin-change barrier, *Phys. Chem. Chem. Phys.* **2016**, *18*, 18137.
- [30] N. Kitagawa, M. Obata, T. Oda, Density functional study on positively charged six-coordinate FeO₂ porphyrin complex for a trigger of O₂ dissociation, *Chem. Phys. Lett.* **2016**, *643*, 119.
- [31] T. Yang, M. G. Quesne, H. M. Neu, F. G. C. Reinhard, D. P. Goldberg, S. P. de Visser, Singlet versus triplet reactivity in an Mn(V)-Oxo species: Testing theoretical predictions against experimental evidence, *J. Am. Chem. Soc.* **2016**, *138*, 12375.
- [32] O. S. Siig, K. P. Kepp, Iron (II) and iron(III) spin crossover: Toward an optimal density functional, *J. Phys. Chem. A* **2018**, *122*, 4208.
- [33] A. Lábás, D. K. Menyhárd, J. N. Harvey, J. Oláh, First principles calculation of the reaction rates for ligand binding to myoglobin: The cases of NO and CO, *Chem. Eur. J.* **2018**, *24*, 5350.
- [34] D. Kurokawa, J. S. Gueriba, W. A. Diño, Spin-dependent O₂ binding to hemoglobin, *ACS Omega* **2018**, *3*, 9241.
- [35] Q. M. Phung, K. Pierloot, The dioxygen adducts of iron and manganese porphyrins: electronic structure and binding energy, *Phys. Chem. Chem. Phys.* **2018**, *20*, 17009.
- [36] L. Du, F. Liu, Y. Li, Z. Yang, Q. Zhang, C. Zhu, J. Gao, Dioxygen activation by iron complexes: The catalytic role of intersystem crossing dynamics for a heme-related model,

J. Phys. Chem. C **2018**, *122*, 2821.

[37] B. Yang, L. Gagliardi, D. G. Truhlar, Transition states of spin-forbidden reactions, *Phys. Chem. Chem. Phys.* **2018**, *20*, 4129.

[38] T. Takayanagi, T. Nakatomi, Automated reaction path searches for spin-forbidden reactions, *J. Comp. Chem.* **2018**, *39*, 1319.

[39] K. Saito, Y. Watabe, T. Fujihara, T. Takayanagi, J. Hasegawa, Spin-inversion mechanisms in O₂ binding to a model heme complex revisited by density function theory calculations, *J. Comp. Chem.* **2020**, *41*, 1130.

[40] T. J. Penfold, E. Gindensperger, C. Daniel, C. M. Marian, Spin-vibronic mechanism for intersystem crossing, *Chem. Rev.* **2018**, *118*, 6975.

[41] H. Ando, S. Iuchi, H. Sato, Theoretical study on ultrafast intersystem crossing of chromium(III) acetylacetonate, *Chem. Phys. Lett.* **2012**, *535*, 177.

[42] C. Lévêque, R. Taïeb, H. Köppel, Theoretical prediction of the importance of the ³B₂ state in the dynamics of sulfur dioxide, *J. Chem. Phys.* **2014**, *140*, 091101.

[43] J. Eng, C. Gourlaouen, E. Gindensperger, C. Daniel, Spin-vibronic quantum dynamics for ultrafast excited-state processes, *Acc. Chem. Res.* **2015**, *48*, 809.

[44] M. Pápai, T. J. Penfold, K. B. Møller, Effect of tert-butyl functionalization on the photoexcited decay of a Fe(II)-N-heterocyclic carbene complex, *J. Phys. Chem. C* **2016**, *120*, 17234.

[45] M. Pápai, G. Vankó, T. Rozgonyi, T. J. Penfold, High-efficiency iron photosensitizer explained with quantum wavepacket dynamics, *J. Phys. Chem. Lett.* **2016**, *7*, 2009.

[46] Y. Harabuchi, J. Eng, E. Gindensperger, T. Taketsugu, S. Maeda, C. Daniel, Exploring the mechanism of ultrafast intersystem crossing in rhenium(i) carbonyl bipyridine halide complexes: key vibrational modes and spin–vibronic quantum dynamics, *J. Chem. Theo. Comp.* **2016**, *12*, 2335.

[47] M. Fumanal, E. Gindensperger, C. Daniel, Ultrafast excited-state decays in [Re(CO)₃(N,N)(L)]ⁿ⁺: Nonadiabatic quantum dynamics, *J. Chem. Theo. Comp.* **2017**, *13*, 1293.

[48] M. J. Frisch, G. W. Trucks, H. B. Schlegel, G. E. Scuseria, M. A. Robb, J. R. Cheeseman, G. Scalmani, V. Barone, B. Mennucci, G. A. Petersson, H. Nakatsuji, M.

Caricato, X. Li, H. P. Hratchian, A. F. Izmaylov, J. Bloino, G. Zheng, J. L. Sonnenberg, M. Hada, M. Ehara, K. Toyota, R. Fukuda, J. Hasegawa, M. Ishida, T. Nakajima, Y. Honda, O. Kitao, H. Nakai, T. Vreven, J. A. Montgomery, jr., J. E. Peralta, F. Ogliaro, M. Bearpark, J. J. Heyd, E. Brothers, K. N. Kudin, V. N. Staroverov, R. Kobayashi, J. Normand, K. Raghavachari, A. Rendell, J. C. Burant, S. S. Iyengar, J. Tomasi, M. Cossi, N. Rega, J. M. Millam, M. Klene, J. E. Knox, J. B. Cross, V. Bakken, C. Adamo, J. Jaramillo, R. Gomperts, R. E. Stratmann, O. Yazyev, A. J. Austin, R. Cammi, C. Pomelli, J. W. Ochterski, R. L. Martin, K. Morokuma, V. G. Zakrzewski, G. A. Voth, P. Salvador, J. J. Dannenberg, S. Dapprich, A. D. Daniels, Ö. Farkas, J. B. Foresman, J. V. Ortiz, J. Cioslowski and D. J. Fox, *Gaussian 09*, Revision D.01, Gaussian, Inc., Wallingford, CT, USA, 2009.

[49] S. Vancoillie, H. Zhao, M. Radoń, K. Pierloot, Performance of CASPT2 and DFT for relative spin-state energetics of heme models, *J. Chem. Theo. Comp.* **2010**, *6*, 576.

[50] C. Angeli, R. Cimiraglia, S. Evangelisti, T. Leininger, J. P. Malrieu, Introduction of n-electron valence states for multireference perturbation theory, *J. Chem. Phys.* **2001**, *114*, 10252.

[51] F. Neese, the ORCA program system, version 4.0. *Comp. Mol. Sci.* **2018**, *8*, e1327.

[52] T. Takayanagi, Y. Watabe, T. Miyazaki, Reduced-dimensionality quantum dynamics study of the $^3\text{Fe}(\text{CO})_4 + \text{H}_2 \rightarrow ^1\text{FeH}_2(\text{CO})_4$ spin-inversion reaction, *Molecules* **2020**, *25*, 882.

[53] F. Neese, Efficient and accurate approximations to the molecular spin-orbit coupling operator and their use in molecular *g*-tensor calculations. *J. Chem. Phys.* **2005**, *122*, 034107.

[54] J. C. Light, I. P. Hamilton, J. V. Lill, Generalized discrete variable approximation in quantum mechanics, *J. Chem. Phys.* **1985**, *82*, 1400.

[55] T.-X. Xie, Y. Zhang, M.-Y. Zhao, K.-L. Han, Calculations of the F + HD reaction on three potential energy surfaces, *Phys. Chem. Chem. Phys.* **2003**, *5*, 2034.

[56] T.-S. Chu, K.-L. Han, Nonadiabatic Time-dependent wave packet study of the $\text{D}^+ + \text{H}_2$ reaction system, *J. Phys. Chem. A* **2005**, *109*, 2050.

[57] N. Balakrishnan, C. Kalyanaraman, N. Sathyamurthy, Time-dependent quantum

- mechanical approach to reactive scattering and related processes, *Phys. Rep.* **1997**, *280*, 79.
- [58] G. Nyman, H.-G. Yu, Quantum theory of bimolecular chemical reactions, *Rep. Prog. Phys.* **2000**, *63*, 1001.
- [59] D. A. Fedorov, S. R. Pruitt, K. Keipert, M. S. Gordon, S. A. Varganov, Ab initio multiple spawning method for intersystem crossing dynamics: spin-forbidden transitions between 3B_1 and 1A_1 States of GeH₂, *J. Phys. Chem. A* **2016**, *120*, 2911.
- [60] D. A. Fedorov, A. O. Lykhin, S. A. Varganov, Predicting intersystem crossing rates with AIMS-DFT molecular dynamics, *J. Phys. Chem. A* **2018**, *122*, 3480.
- [61] R. R. Zaari, S. A. Varganov, Nonadiabatic transition state theory and trajectory surface hopping dynamics: intersystem crossing between 3B_1 and 1A_1 states of SiH₂, *J. Phys. Chem. A* **2015**, *119*, 1332.
- [62] M. Fumanal, E. Gindensperger, C. Daniel, Ultrafast Excited-State Decays in [Re(CO)₃(N,N)(L)]ⁿ⁺: Nonadiabatic Quantum Dynamics, *J. Chem. Theo. Comp.* **2017**, *13*, 1293.

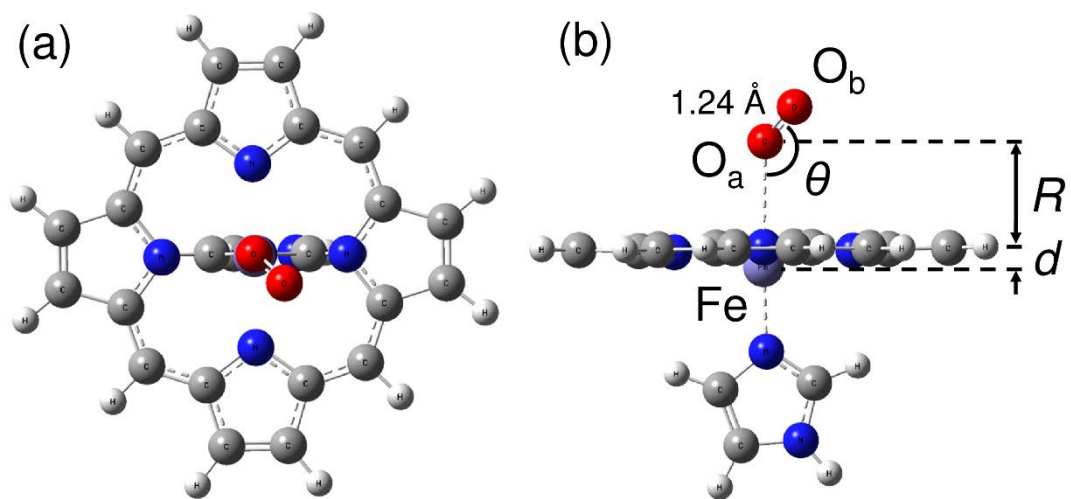


Figure 1

(a) Structure of porphyrin moiety including imidazole and O₂. (b) Definition of the three active coordinates (R , θ , d) used in wave packet dynamics.

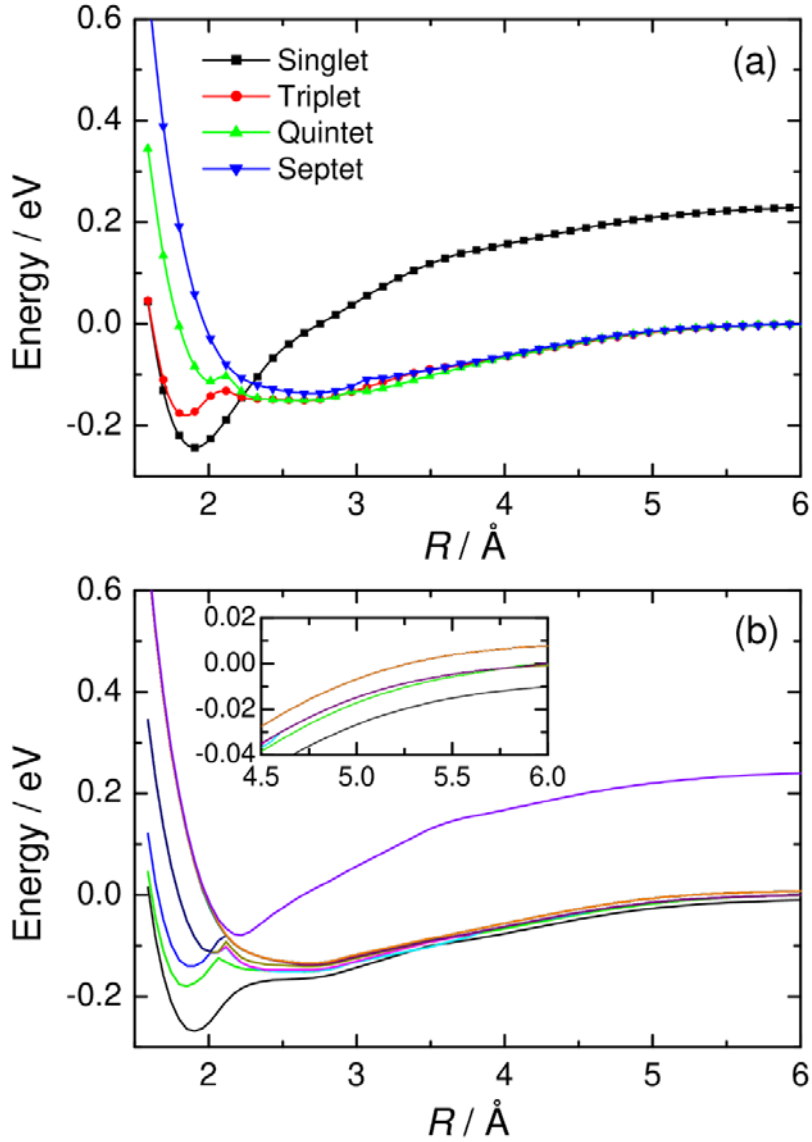


Figure 2

(a) One-dimensional potential energy curves of FePorIm-O₂ in the singlet, triplet, quintet, and septet states as a function of R . (b) One-dimensional adiabatic potential energy curves for 16 spin states including spin-orbit couplings. The inset shows the enlarged plot in the asymptotic region. In both cases, the other two structural parameters, θ and d , are fully optimized with respect to energy.

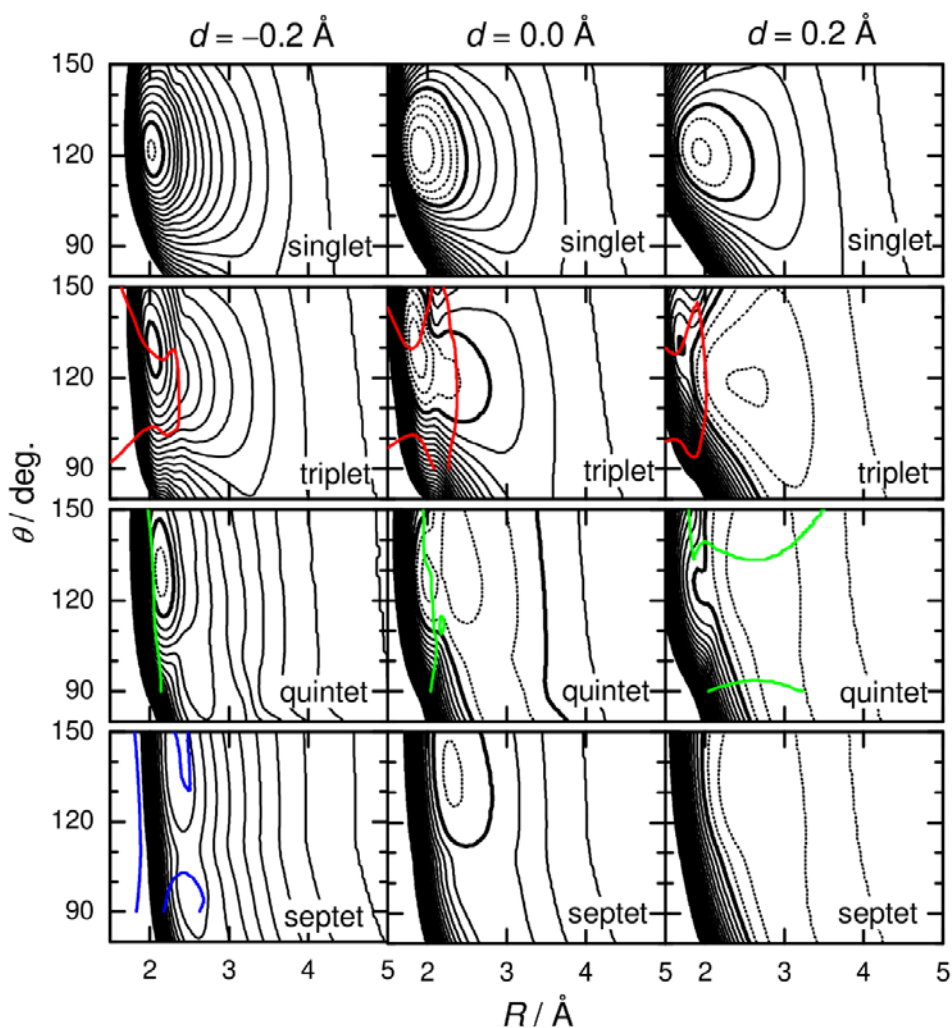


Figure 3

Two-dimensional contour plots of the singlet, triplet, quintet, and septet potential energy surfaces for the FePorIm-O₂ model as a function of (R, θ) with three values of d . The contour increment is 0.05 eV. Zero contours are shown by bold black lines. Dotted and solid thin contours indicate negative and positive contours, respectively. Bold red, green, and blue lines correspond to singlet-triplet, triplet-quintet, and quintet-septet crossing seams, respectively.

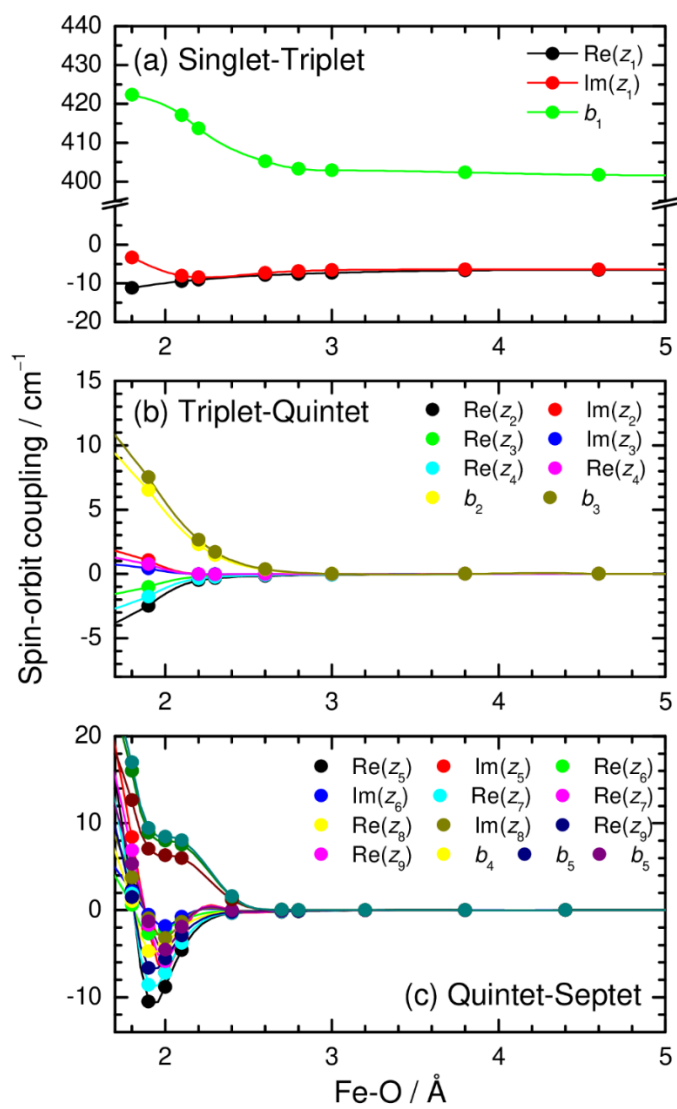


Figure 4

Spin-orbit couplings plotted as a function of Fe-O ($= R + d$) distance. The coupling values are calculated at the state-averaged CASSCF(8_e, 7_o)/def2-TZVP level.

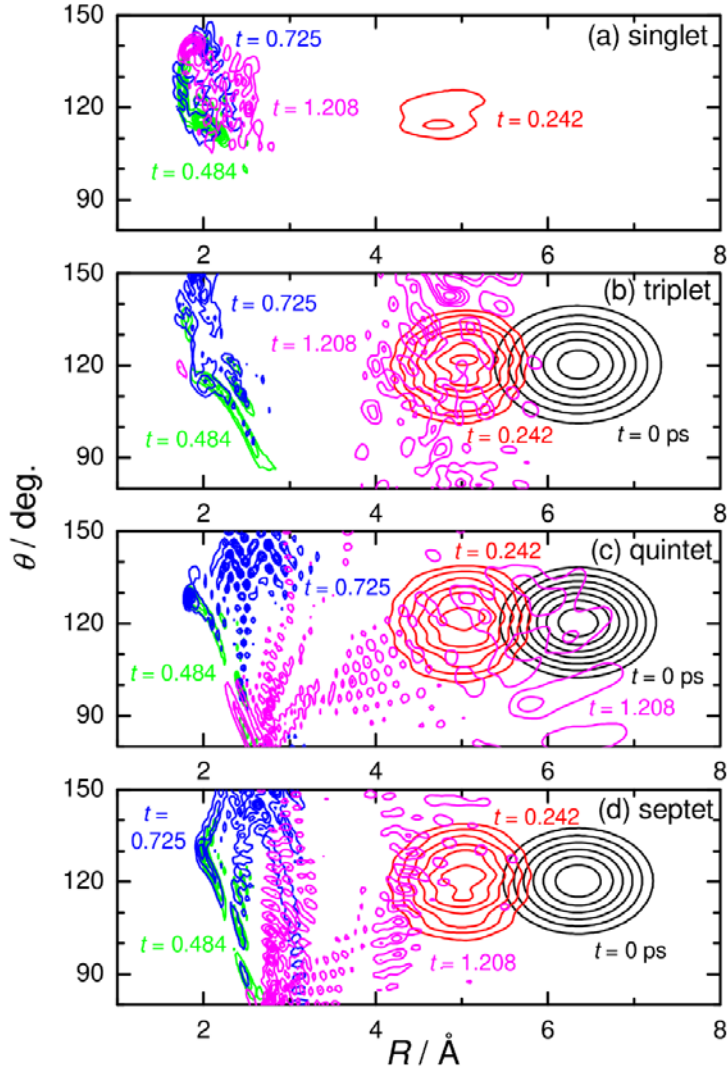


Figure 5

Snapshots of the wave packet probability densities plotted as a function of (R, θ) at an average collision energy of $E = 0.123$ eV (0.005 au) eV. For the triplet, quintet, and septet states, the corresponding probability density is summed over all M_s contributions. The initial wave packet parameters are $(R_0, \theta_0, d_0, a_R, a_\theta, a_d) = (6.35 \text{ \AA}, 120^\circ, 0.16 \text{ \AA}, 0.2 \text{ au}, 6, 0 \text{ au}, 30.0 \text{ au})$ (see Eq. (7)).

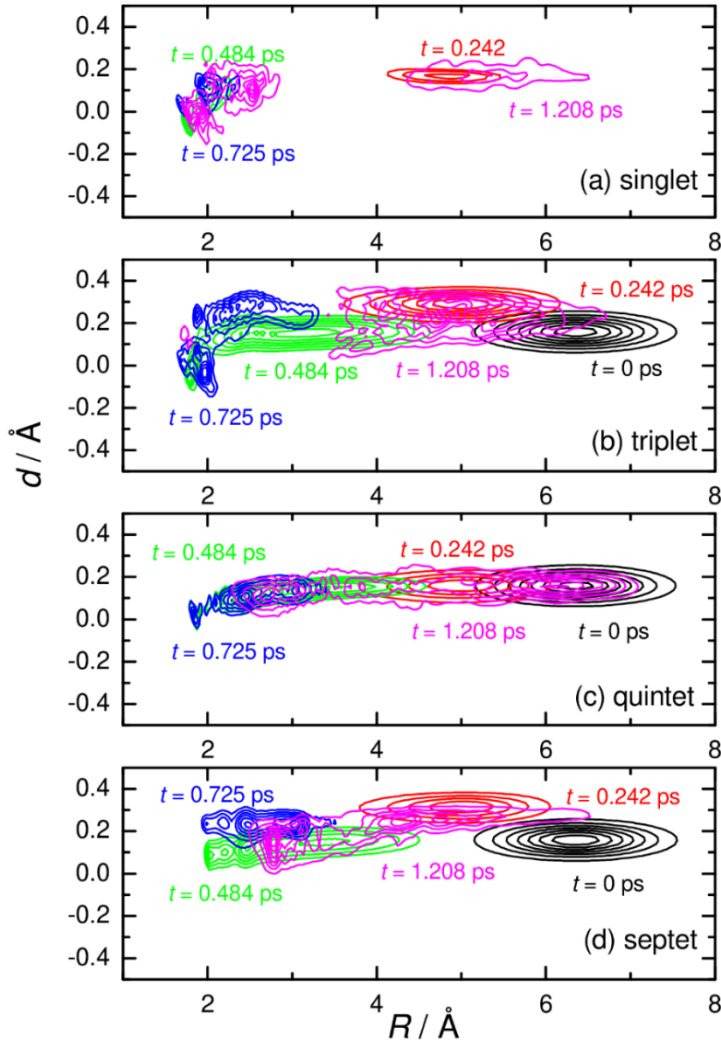


Figure 6

Snapshots of the wave packet probability densities plotted as a function of (R, d) at an average collision energy of $E = 0.123$ eV (0.005 au) eV. For the triplet, quintet, and septet states, the corresponding probability density is summed over all M_s contributions. The initial wave packet parameters are $(R_0, \theta_0, d_0, a_R, a_\theta, a_d) = (6.35 \text{ \AA}, 120^\circ, 0.16 \text{ \AA}, 0.2 \text{ au}, 6, 0 \text{ au}, 30.0 \text{ au})$ (see Eq. (7)).

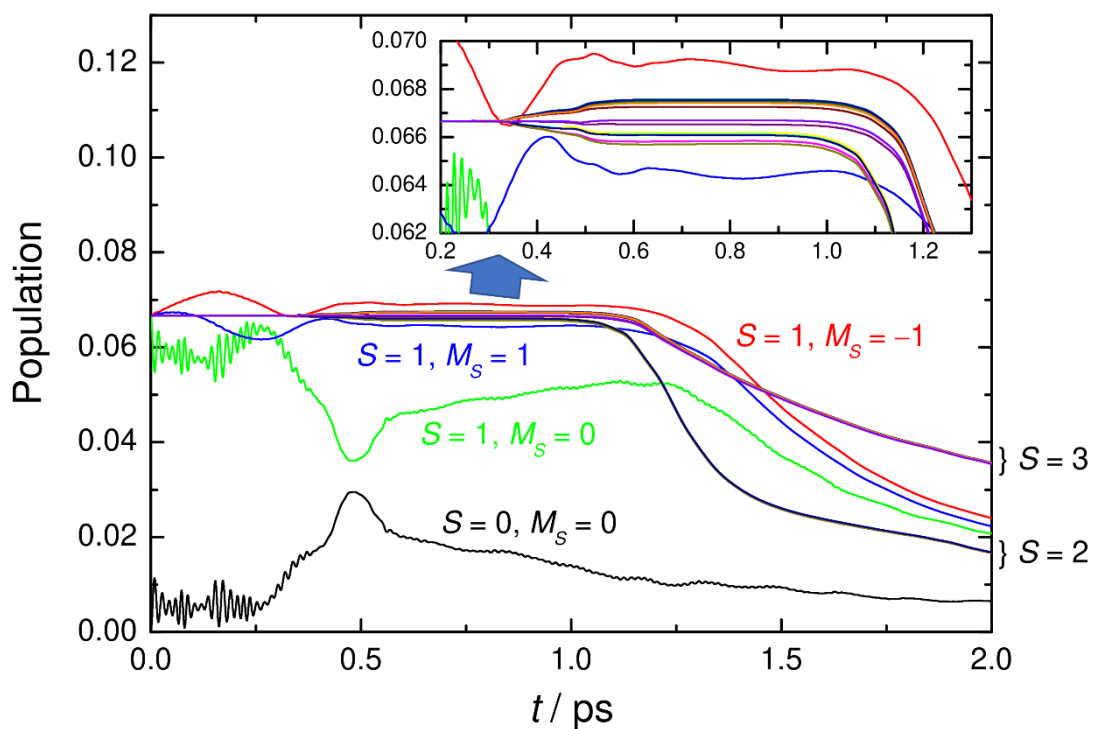


Figure 7

Time evolution of the wave packet population on the spin diabatic state obtained from the 16-spin state nonadiabatic calculations. The initial diabatic populations are set to $c_1 = 0$ and $c_i = 1/15$ ($i = 2-16$). The inset shows the enlarged plot.

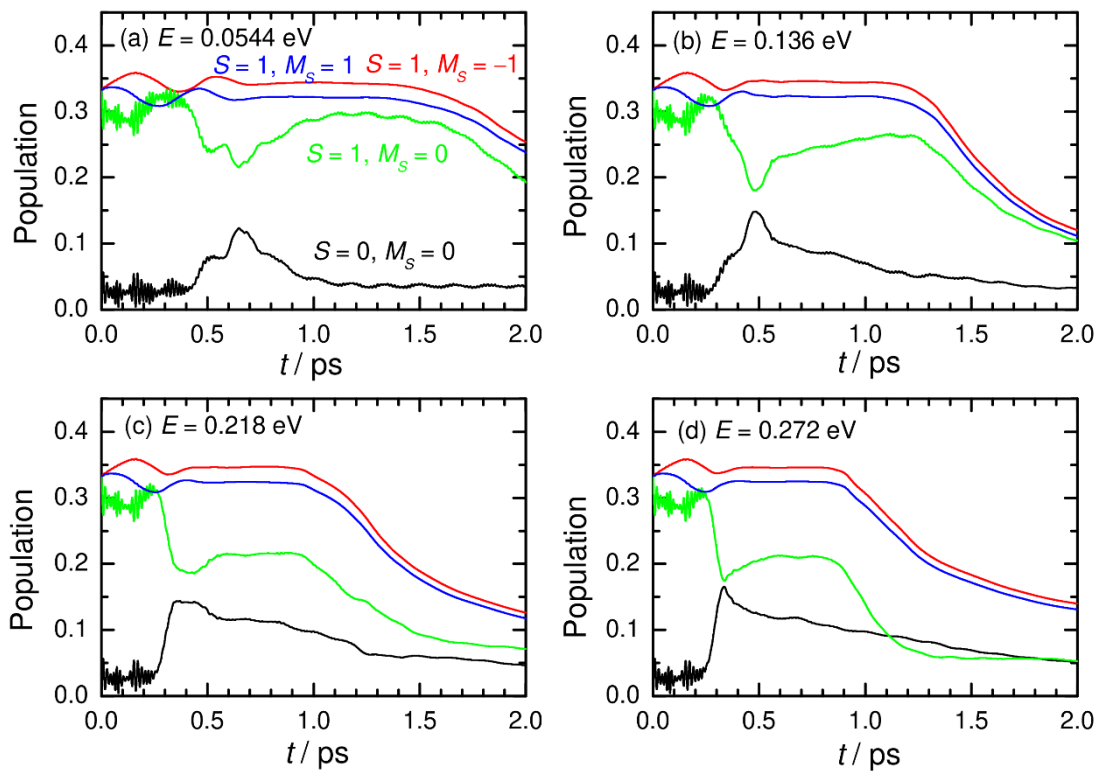


Figure 8

Time evolution of the wave packet population on the spin diabatic state obtained from the four-spin state nonadiabatic calculations. The initial diabatic populations were set to $c_1 = 0$ and $c_i = 1/3$ ($i = 2-4$).

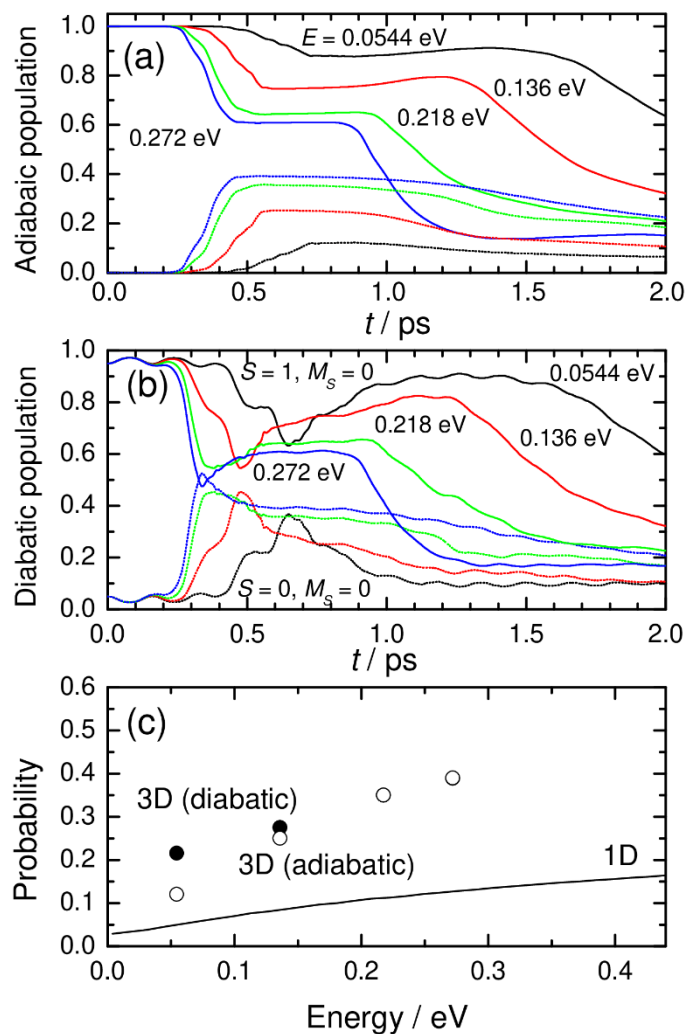


Figure 9

(a) Time evolution of the wave packet populations on the two spin adiabatic states obtained from the four-spin state nonadiabatic calculations, where the initial population on the lowest adiabatic state was set to unity. The calculations are done at four collision energies. (b) Time evolution of populations on the singlet ($S = M_s = 0$) and triplet ($S = 1$ and $M_s = 0$) diabatic states. (c) Comparison of singlet production probabilities as a function of collision energy. Open and closes circles are from the adiabatic and diabatic analyses of the 3D wave packet calculations, respectively. Solid line is corresponding to the one-dimensional result (see text).